The Impact of X-Ray Radiation on Chemical and Optical Properties of Triple-Cation Lead Halide Perovskite: from the Surface to the Bulk

Guillaume Vidon, Pia Dally, Mirella Al-Katrib, Daniel Ory, Minjin Kim, Etienne Soret, Eva Rangayen, Marie Legrand, Alexandre Blaizot, Philip Schulz, et al.

▶ **To cite this version:**

Guillaume Vidon, Pia Dally, Mirella Al-Katrib, Daniel Ory, Minjin Kim, et al.. The Impact of X-Ray Radiation on Chemical and Optical Properties of Triple-Cation Lead Halide Perovskite: from the Surface to the Bulk. Advanced Functional Materials, 2023, 10.1002/adfm.202304730 . hal-04180582

HAL Id: hal-04180582
https://hal.science/hal-04180582v1

Submitted on 14 Nov 2024

HAL is a multi-disciplinary open access archive for the deposit and dissemination of scientific research documents, whether they are published or not. The documents may come from teaching and research institutions in France or abroad, or from public or private research centers.

L'archive ouverte pluridisciplinaire **HAL**, est destinée au dépôt et à la diffusion de documents scientifiques de niveau recherche, publiés ou non, émanant des établissements d'enseignement et de recherche français ou étrangers, des laboratoires publics ou privés.

The impact of X-ray radiation on chemical and optical properties of triple-cation lead halide perovskite: from the surface to the bulk

*Guillaume Vidon+, Pia Dally+, Mirella Al-Katrib, Daniel Ory, Minjin Kim, Etienne Soret, Eva Rangayen, Marie Legrand, Alexandre Blaizot, Philip Schulz, Jean-Baptiste Puel, Daniel Suchet, Jean-François Guillemoles, Arnaud Etcheberry, Muriel Bouttemy, Stefania Cacovich**

Dr. G. Vidon, Dr. M. Kim, E. Soret, Dr. P. Schulz, Dr. D. Suchet, Dr. J.F. Guillemoles, Dr. S. Cacovich
Institut Photovoltaïque d'Ile-de-France (IPVF), UMR 9006, CNRS, Ecole Polytechnique, IP Paris, Chimie Paristech, PSL, 91120 Palaiseau, France
E-mail: stefania.cacovich@cnrs.fr

Dr. P. Dally, Dr. M. Al-Katrib, Dr. A. Etcheberry, Dr. M. Bouttemy
Institut Lavoisier de Versailles (ILV), Université de Versailles Saint-Quentin-en-Yvelines, Université Paris-Saclay, CNRS, UMR 8180, 45 avenue des Etats-Unis, 78035 Versailles CEDEX, France

Dr. D. Ory, Dr. M. Legrand, J.B. Puel
Électricité de France (EDF), R&D, 18 Boulevard Thomas Gobert, Palaiseau 91120, France

Dr. P. Dally, Dr. M. Al-Katrib, Dr. D. Ory, E. Rangayen, Dr. M. Legrand, A. Blaizot, J.B. Puel, Dr. M. Bouttemy
Institut Photovoltaïque d'Île-de-France (IPVF), 18 Boulevard Thomas Gobert, Palaiseau 91120, France

Keywords: X-rays, Halide Perovskites, Photoluminescence Imaging, X-ray Photoemission Spectroscopy, Time-resolved Spectroscopy

Abstract

Understanding the effects of X-rays on halide perovskite thin films is critical for accurate and reliable characterization of this class of materials, as well as their use in detection systems. In this work, we employ advanced optical imaging techniques, both spectrally and temporally resolved, coupled with chemical characterizations to obtain a comprehensive picture of the degradation mechanism occurring in the material during photoemission spectroscopy measurements. Two main degradation pathways were identified through the use of local correlative physico-chemical analysis. The first one, at low X-Ray fluence, shows minor changes of the surface chemistry and composition associated with the formation of electronic defects. Moreover, a second degradation route occurring at higher fluence leads to the evaporation of the organic cations and the formation of an iodine-poor perovskite. Based on the local variation of the optoelectronic properties, a kinetic model describing the different mechanisms is proposed. These findings provide valuable insight on the impact of X-rays on the perovskite layers during investigations using X-ray based techniques. More generally, a deep understanding of the interaction mechanism of X-rays with perovskite thin films is essential for the development of perovskite based X-ray detectors and solar for space applications.

1. Introduction

X-ray stability of material and devices when exposed to X-rays irradiation is a fundamental topic that lies at the interface of solid-state chemistry, metrology and application issues. This work focuses on the case of halide perovskites which have proven to be a very promising class of materials for multiple optoelectronic applications ranging from earth-based solar cell application[1], space-based solar cells[2,3], LED[4], laser emission[5] or even X-ray detection[6,7]. Perovskite based X-ray detectors have demonstrated potential applications in fields such as medical imaging, radiation dosimetry, and nuclear security[8–10]. However, perovskite based X-ray detector technology is still in the early stages of development and more research is needed to fully understand the complex behaviour of perovskites under continuous and long time X-ray irradiation.

In addition, X-ray irradiation, as a perturbation factor, is crucial due to its use in numerous material characterization methods. X-ray diffraction (XRD), including conventional laboratory based XRD or synchrotron-based grazing-incidence wide-angle x-ray scattering[11], is one of the most prominent of these methods. Regarding chemical surface characterization of

perovskites, X-ray photoelectron spectroscopy (XPS) is a common and robust technique[12] nowadays widely used.

The degradation of the perovskite layers toward X-rays during XPS analyses has previously been reported, particularly when photoemission spectroscopy is operated with synchrotron sources whose fluence is even brighter than that of laboratory sources[13,14]. Importantly, the chemical composition of the perovskite layer has a direct effect on its stability under X-ray. In the case of methylammonium lead iodide, or MAPI ($CH_3NH_3PbI_3$), a relatively poor stability [15] has been demonstrated while their inorganic counterparts appear to be more stable[14,16]. Indeed, it was shown that MAPI tends to form side PbI_2, which then further partly decomposes into metallic lead Pb^0 [17–19]. In their work, Steirer et al[15,20] studied the defect tolerance in MAPI perovskite under X-rays and found that the changes in composition begin immediately with exposure to X-ray irradiation, with a severe loss of MA^+ and a side formation of PbI_2 after several hours of exposure. We are therefore confronted with valuable characterization techniques based on X-rays which unfortunately induce involuntary degradation. Accurate understanding of the effects of X-rays on halide perovskite materials is thus crucial for the interpretation of chemical analysis by XPS and by other X-ray based techniques. This meets the fundamental question regarding the nature of the instability of perovskite lattices[11]. The issue becomes even more pressing when considering the reliability of *operando* experiments, where the materials are exposed to high X-rays fluxes for a long duration[21,22].

In their work[14], Svanstrom et al. tackled the question of the impact of X-ray based techniques on organic-inorganic lead halide perovskites using hard X-ray photoelectron spectroscopy with fluences of the order of [10^{18} ; 10^{20}] ph/cm². They evidenced two degradation pathways: the decomposition of the lead halide cage and the degradation of the organic elements of the perovskite. Recently, Orri et al.[23] described the impact of electron beam and X-ray beam damage at the nanometer scale on perovskite layers. They evidenced Iodine segregation towards the grain boundaries and the formation of both $PbBr_2$ and PbI_2 at the grain boundaries.

Here, we go further in the analysis of such mechanisms and we study the impact of X-ray exposure in the range of 10^{13} ph/cm²/s during XPS surface analysis on triple cations perovskite not only showing the chemical evolution of the perovskite surface under X-rays but also the impact on the optical properties. The added-value of this study lies in the combination of two characterization techniques, XPS and photoluminescence, that probe different depths of the perovskite layer and bring complementary chemical and optical information to better understand the degradation mechanism. XPS is thus used to generate irradiated areas for the study and for surface analysis of the perturbed perovskite layer, serving as both the perturbation

source and the analytic technique to monitor chemical changes. Importantly, advanced steady state and time resolved imaging methods were employed to systematically track the local evolution of bulk and surface carrier recombination, providing novel insights on the interaction mechanism between X-rays and halide perovskites from an optical standpoint. We obtained three main results. One, we confirmed that X-rays do cause a reproducible chemical modification of the surface of the perovskite layer with degradation of the organic and iodine components and formation of metallic lead. Two, this modification comes with the creation of electronic defects both in the bulk and at the surface that are spatially non uniform. Three, the X-rays also cause the formation of a I-poor perovskite region that is itself reactive with the X-rays with a reaction diagram that we deduce from photoluminescence imaging analysis.

2. Results

2.1 Monitoring surface chemical modification of the metal halide perovskite (MHP) layer under X-rays irradiation

The studied sample is a half-cell constituted of a stack of triple cation double halide perovskite with a stoichiometry of $Cs_{0.05}(MA_{0.14}, FA_{0.86})_{0.95} Pb(I_{0.84}, Br_{0.16})_3$ deposited on glass / fluorine doped tin oxide (FTO) / compact titanium oxide (c-TiO_2). The kinetic of degradation and associated chemical evolution of the perovskite layer inside the XPS X-ray spot were studied by proceeding to XPS acquisition (so, under UHV) at the same position, for irradiation duration until 1, 2, 4, 8 and 16h exposition corresponding to the 5 different spots of the same sample schematized in **Figure 1(a)**.

Homogeneity of the sample composition was first verified by analysing 4 spots distributed randomly. In **Figure S1,** XPS high-resolution spectra of C 1s, N 1s, Pb 4f, Cs 3d, Br 3d and I 3d, for the studied spots, are presented showing the same intensity and same energy distribution, i.e. the same chemical environments, meaning a great chemical homogeneity of the surface, a crucial information for the robustness of the combined chemical and optical studies. With present acquisition sequence, previously optimised for triple cations perovskite [24], the minimal exposition duration is 1h which corresponds to the time necessary to measure all the high resolution photopics and the two control surveys, one at the beginning and another in the end. Consequently, this configuration offers the possibility to track hour by hour the chemical modification all along the exposition to X-ray.

During this first 1h analysis, survey spectra of 4 min duration are sequentially recorded in order to have access to the eventual evolution of the elemental composition. As shown in **Figure 1(b)** the elemental composition for the time "0" (real time 4 min) or 1h are the same and coherent with the expected composition of the MHP. The slight global differences between the 5 spots are linked to the adventitious carbon screening that is not exactly the same all over the sample surface. Afterwards at 1h exposure, the high resolution core levels are recorded.

The evolution of the atomic percentage of the perovskite elements (Pb, I, C, N, Br, Cs and O) obtained from the survey spectra on the 5 spots are presented in **Figure 1(b)**. We note that the chemical composition reported for t=0 is the one obtained from the first survey spectra (total duration of analysis is 4 min). By comparing this evolution, we can clearly observe that the perovskite surface composition evolution follows two concomitant behaviours under X-ray irradiation. The first one, specific to the organic compound of the perovskite, associated to C and N species, shows a progressive and significant decrease after the first 1h of X-ray exposure with a more pronounced decrease between 2h and 12h. The second, related to the inorganic compounds, more precisely I, Pb and Br elements, shows a visible increase of their atomic percentage along the exposure duration. These trends are perfectly reproducible, and demonstrated by the exact same evolution of the elemental composition for the same X-ray exposure duration for the 5 different spots.

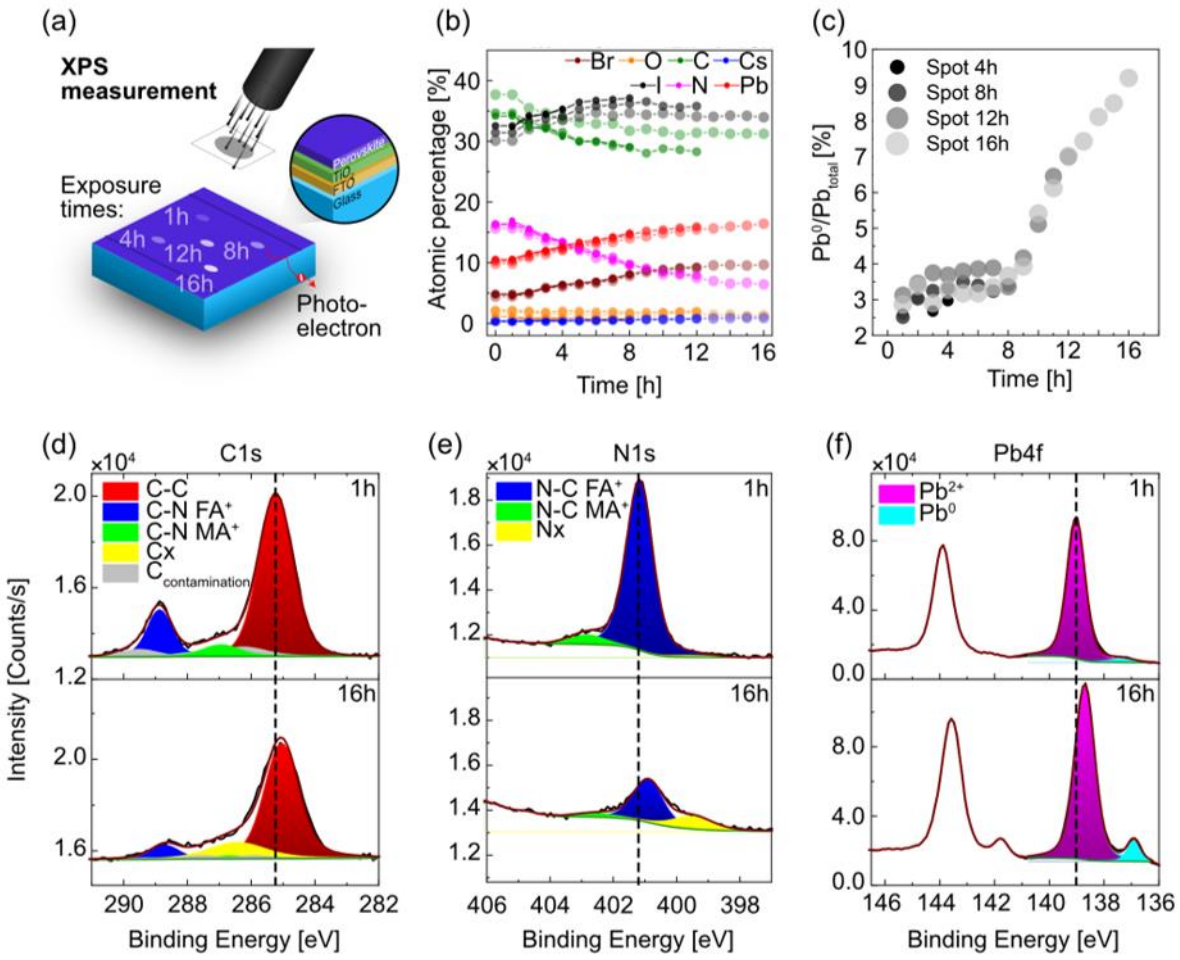

Figure 1. (a) Summary diagram of the study: XPS spectrometer used as irradiation source (X-ray gun) and analysis tool. 5 different X-ray exposure durations on a single sample composed by a stack of glass/FTO/TiO_2/MPHP are studied. (b) Evolution of atomic percentage of perovskite elements for the different exposure time from 1h to 16h for the 5 spots (survey spectra for 1h, 4h, 8h, 12h and 16h spot). (c) Evolution of Pb^0 / Pb_{total} contribution ratio along the exposure time for the spots 4h, 8h, 12h and 16h. (d-f) High resolution spectra of C 1s, N 1s and Pb 4f for the extreme X-ray exposure time of 1h and 16h acquired on the same spot. The vertical dashed lines are drawn to witness the shift in the binding energy position of each core level between the first scan at 1h and the last scan at 16h.

In **Figure 1(f)** we show the high resolution spectra of Pb $4f_{7/2}$ for 1h and 16h of exposure measured on the same spot. Initially, Pb $4f_{7/2}$ core level showed one single peak at 139.0 eV attributed to Pb^{2+} resulting from Pb - I bond. After 16h of X-ray exposure, significant Pb^0 contribution is present at lower binding energy (136.9 eV) indicating the presence of metallic lead states associated with small Pb metallic clusters, as also previously reported [14,25]. From the fit of these two contributions, the ratio of Pb^0 / Pb_{total} along the exposure time for the 5

measured spots is shown in **Figure 1(c)**. Between 1h and 8h of continuous X-rays exposure, the evolution of Pb^0 / Pb_{total} ratio does not exceed 4 %, an identical trend reported on the 5 spots for the same exposure time (1h, 4h and 8h). After 8h, the formation of Pb^0 becomes progressively more important for the two spots, reaching up to 9 % after 16h. The superposition of the 5 curves of Pb^0 evolution, corresponding to 5 different spots of the sample, shows again a high level of reproducibility of the degradation phenomenon, from intensity and kinetic point of view. This indicates that the X-ray induced surface chemical changes are the same everywhere, regardless of where the measurement is carried out on the sample, further validating our experimental procedure as well as the following photoluminescence analysis.

To have more insight into the impact of X-rays on the organic matrix of the perovskite, we studied the changes in the core levels of C 1s and N 1s between 1h and 16h on the same spot. Spectra shown in **Figure 1(d)** and **1(e)** reveal significant modifications between 1h and 16h not only of the intensity, but also of the chemistry. In the C 1s core level, the peak at 284.9 eV attributed to the carbon contamination, decreases progressively (not shown here) until 16h of X-ray exposure as an effect of the ultra-high vacuum environment during the analysis. In addition, the peak at 288.9 eV, attributed to the C = N bond in the FA^+ contribution, shows a very significant decrease in intensity. Moreover, the peak at 286.5 eV attributed to the C - N bond in the MA+ contribution becomes difficult to analyse due to its very low remaining contribution and the presence of C - O contamination at almost the same binding energy. As for the N 1s core level, we observed the same behaviour illustrated by the decrease of the peaks at 401.2 eV and 402.6 eV corresponding to FA^+ and MA^+ contributions, respectively. Another observed change relative to the organic cations is highlighted by the appearance of new side peaks on both the C 1s and N 1s spectra at about 287.0 eV and 399.8 eV, respectively. These new species, labelled as Cx and Nx, are most probably linked to the formation of a fewer volatile species under UHV conditions [26], most clearly seen for the highest X-ray exposure, 16h. Note that we observe a similar trend with the present FA^+ dominant perovskite compared with the study of Sterier et al.[15] dealing with a MAPI active layer

In addition to the simultaneous degradation of FA^+ and MA^+, and formation of these new C_x and N_x less volatile organic species, a shift toward lower binding energies is also observed between 1h and 16h. This shift is also observed for all the core levels, as reported in **Figure S2 (a-c)**, where the high resolution spectra for I 3d, Br 3d and Cs 3d are presented for all the studied X-ray exposure time. In a general way, when shifts in the binding energies of a core level are

observed it could be related to the changes in the chemical environment of this element. Nevertheless, this doesn't seem to be the case here, since the shift is noticed for all the core levels, including the C-C carbon contamination, and thus could be more probably attributed to a Fermi level pinning of the surface associated with the formation of metallic lead states at the surface [26–28]. This binding energy shift between 1h and 16h is reported in **Figure S2 (d)** showing that the valence band (VB) and FA^+ peak present the same shift ($\Delta eV = 0.20$ eV) as the one observed for the carbon contamination considered as a reference peak. The shift observed for the inorganic matrix, represented by I, Pb and Br [15,20] seemed to be higher, about 0.33 eV so that it must be considered as significant, showing a different behaviour of the inorganic cluster.

2.2. X-rays caused defects that are not spatially uniform

Nevertheless, the degradation mechanisms of the bulk of the perovskite absorber cannot be probed by XPS analysis, as such characterisation technique is limited to the first 5-10 nm of the surface of the samples. In order to gain further insights on the effect of X-rays deeper in the thin films and investigate their impact on local optical properties, we combined temporally[29] and spectrally[29,30] resolved photoluminescence (PL) imaging measurements which are non-destructive techniques. A set of 5 spots corresponding to the 5 expositions duration was prepared in identical conditions for this complementary study. All PL experiments were performed in nitrogen atmosphere to avoid light soaking effects[31].

In **Figure 2**, we present evidence of the optical degradation of the perovskite layers as a result of their exposure to X-rays. Each column corresponds to a duration of exposure to the X-ray beam during the XPS experiment. **Figure 2(a)** shows hyperspectral maps of luminescence intensity at the perovskite peak wavelength of 760 nm. Moreover, in **Figure 2(c)** we show the local spectra taken inside the defect zone as a function of wavelength for different X-ray exposure times. We observe that the intensity of steady-state PL inside the spot zone is reduced by at least a factor five compared to the unaffected zone. Notably, even 1h of exposure to X-ray is enough to induce visible degradation in the photoluminescence images, suggesting that most of the damage in terms of electronic defects occurs within the first hour of beam exposure. Indeed, XPS surface analysis showed no significant change in the chemical composition before and after 1h of X-ray exposure as well as no major modifications in the chemical environment of the elements until 8h of continuous radiation. Hence, the modifications observed in PL after 1h of X-ray radiation are likely to be mainly occurring in the bulk of the perovskite layer and

not on the surface. Metallic lead clusters, which can act as recombination centres, were evidenced at the surface in **Figure 1(c)** only after 8h of exposure. Another remarkable feature of these curves is that the luminescence inside the spot is not decreasing drastically as the X-ray fluence increases. Interestingly, we do not observe a perfect ellipse for the degraded perovskite phase (**Figure 2 (a)** and **(b)**). We attribute this asymmetry to the 60° angle between the X-ray source and the surface normal.

We plot in **Figure 2(b)** the decay times of the degraded zones obtained by Time Resolved - FLuorescence IMaging (TR-FLIM) acquisitions. Local time resolved decays inside the spot are shown in **Figure 2(d).** The decays follow two main dynamics. The first one, at short time ($t<50ns$), varies with the X-ray exposure time. We interpret the short time dynamics as being related to surface defects that would increase with the X-ray exposure time. This will be more precisely studied with the λ-TRFLIM (wavelength dependent) results presented later that do suggest the presence of surface defects in the centre of the X-ray spot. A second dynamic, at long time decays ($t>150ns$) seem rather independent of the X-ray exposure time and of similar order of magnitude as the decay time outside of the affected zone. We think that this surprisingly high decay time - even for the 16h exposed spot - relates to perovskite clusters that would somehow "resist" to the degradation. This observation correlates well with the XPS data of **Figure 1** where, even after 16h of exposure, the signal from the perovskite is still detected.

To compare the information of hyperspectral maps and decay times maps, one can consider that the hyperspectral maps are proportional to the product of absorptivity times decay time. Thereby, any change between the map of decay time and the map of hyperspectral emission can be analysed in terms of absorption. We do see differences (mainly for the 8-16h maps) when comparing the ratio of values inside and outside the spot (see **Figure S4**): the ratio of decay times is higher than for hyperspectral intensity. We think that differences in terms of absorption should therefore occur between the different spots and might be related to the presence of an additional emissive phase that will be discussed in detail in **Section 2.3**.

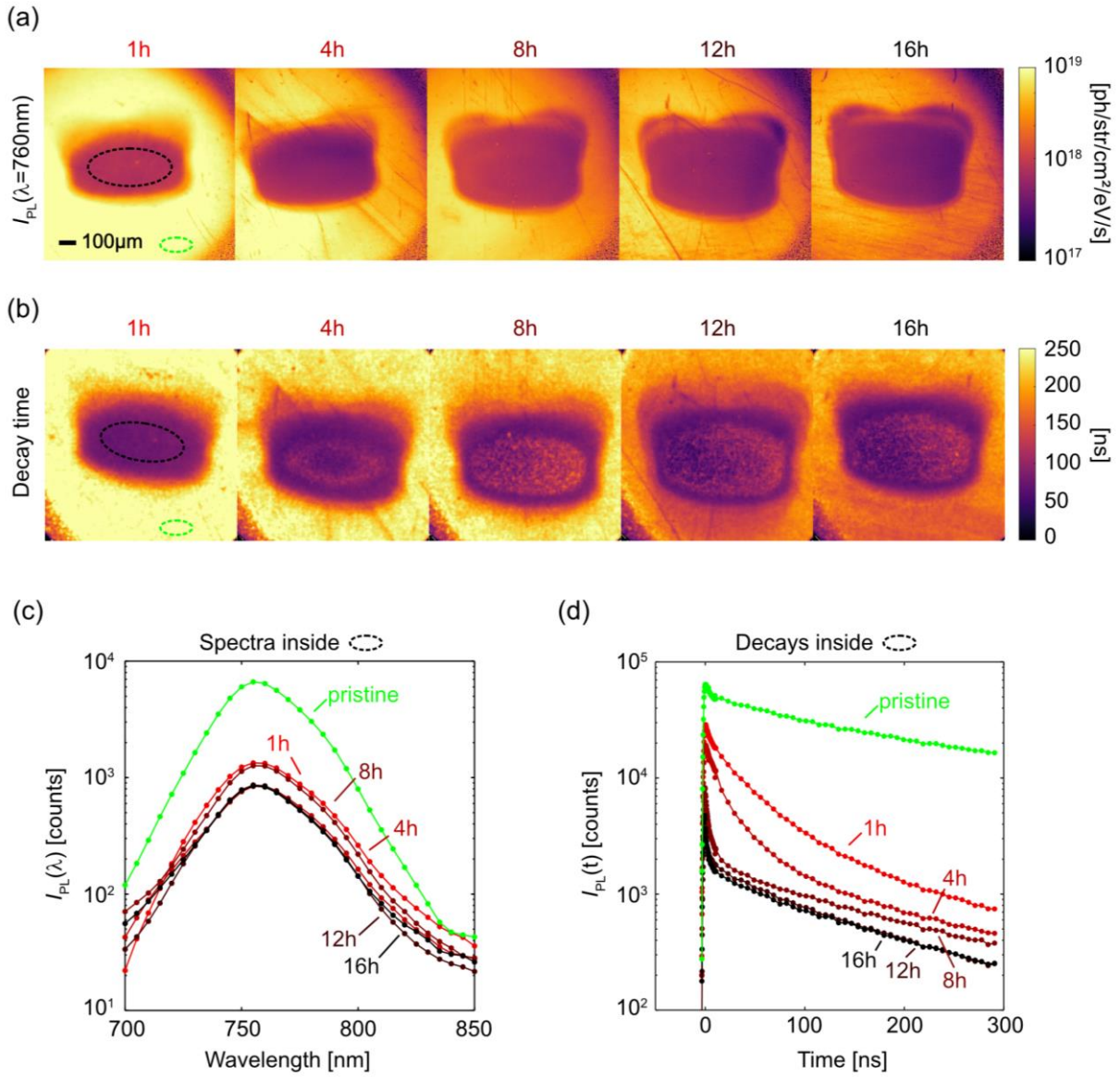

Figure 2: Degradation of the perovskite opto-electronic properties at different X-ray exposure times. (a) PL intensity maps at 760 nm from the steady-state experiment (b) Decay time fitted between *t*=100ns and *t*=300ns after the laser pulse in the pulsed experiment. The exact same regions are imaged on the two setups. The dotted ellipses represent the regions of interest used for the computation of the averaged spectra and decays. (c) PL spectra inside the damaged area (black ellipse in (a)) and pristine sample (green ellipse in (a)) for different exposure times. (d) Decays inside the damaged area (black ellipse in (b)) and pristine sample (green ellipse in (b)) for different exposure times.

Time-resolved photoluminescence (TR-PL) analysis coupled with physical modelling allows to decorrelate bulk from surface recombination processes. In **Figure 3**, we study the position

of the defects induced by X-rays exposure by correlating TR-PL and spatially resolved XPS measurement. In order to estimate if the defects caused by X-rays are located in the bulk or at the surface[32] we employed a novel method which relies on the observation of the initial derivative of the TR-PL decays for different wavelengths of laser excitation. More details on this method are provided in the Supplementary Information and in[33]. In **Figure 3(a)** we show the map of top surface recombination velocity and in **Figure 3(b)** of bulk recombination lifetime of the 8h spot. Inside the elliptical X-ray spot (zone 1), we observe both an increase of the top surface recombination velocity and a reduction of the bulk decay time. In the near region to the central zone of the spot, the PL modifications imply also side perovskite degradation (see zone 2 in **Figure (3a)** and **(b)**). This effect can have several origins. One could be the imperfect focusing of the X-ray spot, another could arise from the compensation of the photoemission effect by the creation of electrons flow. To correlate this spatialization of defects to the surface chemistry, we performed a spatially resolved XPS measurement. Smaller spot sizes (~50µm) aligned sequentially were used to study, inside and outside the larger elliptic spot (400 x 750 µm), the surface composition of the previously irradiated samples (1h and 16h). For every small spot, a survey spectrum (4 min duration) was recorded to access the elemental composition, along the horizontal axis (larger diagonal of the ellipse, see **Figure S3)**. So, eventual additional X-ray perturbation must be neglected. In **Figure 3(c),** we report the atomic ratios (I + Br) / Pb, I / Br and N / Pb, calculated for every 50µm spot for both X-ray exposure time, 1h (dotted lines) and 16h (full line). We observe that for 1h irradiation spot, the atomic ratios inside the spot are quite identical along the horizontal axis inside and outside the large spot, with values close to the one expected from the nominal stoichiometry of the perovskite $Cs_{0.05}(MA_{0.14}, FA_{0.86})_{0.95}$ $Pb(I_{0.84}, Br_{0.16})_3$ indicating that the surface chemistry is rather unchanged. This result is consistent with previous result obtained when averaging in the whole spot. It also demonstrates that, from a surface chemical point of view, there is no dramatic heterogeneity within the spot area, or these modifications are at the limit of the employed spatial resolution and detection threshold of the "small spot" mode of XPS technique. Nevertheless, the PL signal is visibly and strongly reduced inside the spot, as shown in **Figure 3(d)**. We attribute this difference to the difference of the probed thickness of each technique: bulk for PL and surface for XPS, highlighting that the perovskite degradation occurring after 1h of X-ray exposure is less likely to be happening to the extreme surface but is nonetheless happening in the bulk. Note that considering the estimation of the penetration depth by means of mass attenuation coefficients, the X-ray beam passes through the entire perovskite layer. However, for the 16h spot, the atomic ratios show a significant change between inside the spot (dark

orange area on figure 3(b)), and outside the irradiated spot (light orange area on figure 3(b)). Remarkably, the N / Pb ratio, decreases from 1.6 outside the spot area to 0.2 inside. Interestingly, we noticed that I / Br shows more severe drop (5.5 vs 2.0) between the inside and outside spot zone compared to the (I + Br) / Pb ratio (3.6 vs 2.6), suggesting an apparent I loss. By correlating these ratios with the information extracted from the high-energy spectra measured within the whole spot area, this discrepancy is in line with the formation of Pb^0, whose exact distribution at the surface is not determined (probably clusters dispersed at the surface who tends to collapse in time when the X-ray degradation increases) and the loss of organic species in line with MA^+ and FA^+ progressive elimination from the surface with the X-ray dose[34]. This XPS interpretation does not exclude the presence of such Pb^0 clusters in the bulk. This analysis suggests that, at low fluence (outside of the central spot), X-rays cause the formation of bulk defects, but at higher fluence (inside the central spot), surface recombination is increased. This observation is correlated with the XPS surface analysis that evidenced the formation of Pb^0 and the loss of organic species at the high fluence[34]. The absence of significant chemical evolution outside the spot demonstrates the stability of the perovskite layer toward UHV and highlights the role of X-rays only in the degradation mechanism.

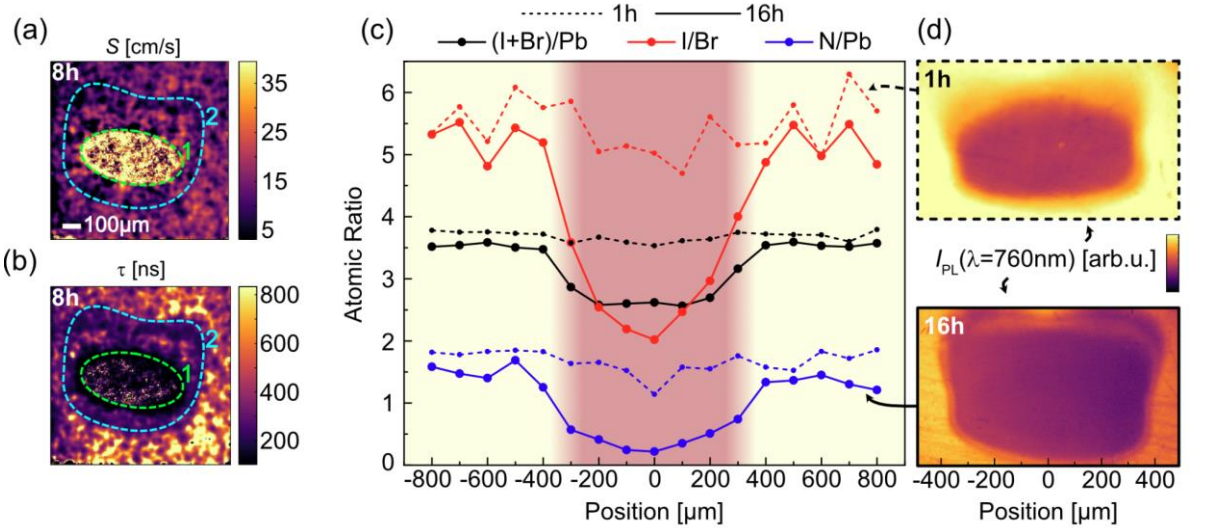

Figure 3: Maps of surface (a) and bulk (b) defect recombination parameters as obtained via the λ-TR-FLIM technique described in the text for the 8h spot. (c) Spatially resolved XPS measurement (with smaller spot size ~50µm). Atomic ratios for the 1h spot (full line) and for the 16h spot (dotted line). (d) Continuous wave PL maps at 760 nm after 1h and 16h of X-rays exposure.

2.3 Formation of a "I-poor" perovskite region that itself reacts with X-rays

The X-ray not only degrades the perovskite by inducing defects but also triggers chemical reactions leading to the formation of new emitting species. In **Figure 4(a)** and **(b)** we show the results of a hyperspectral acquisition of the 16h spot: 3 spectra are plotted in (a) corresponding to the 3 regions of interest shown in circles in (b). We observe that a new peak appears in the centre of the X-ray spot, from approximately 650 nm to 700 nm that is superimposed to the main perovskite emission centred at 760 nm. Then, we performed TR-FLIM analysis by using filters during the acquisition to eliminate the main perovskite peak and to observe the decays in the [610,700] nm range. In **Figure 4(c)** we plot them in three positions similar to the positions in (b). The decays are much faster than those of the main perovskite peak with a loss of two orders of magnitude of PL in ~15 ns compared to >300 ns for the main perovskite peak. In **Figure 4(d)**, we show the local decay time computed in the [3,6] ns interval (only interval with high enough signal to noise ratio). The decay time is reduced as the X-ray exposure time increases. The order of magnitude of the decay times are 1 to 10 ns. These low decay times may originate from charge transfer to the lower bandgap phase[36,37]. We also observe that the spatial repartition of decay times evolves from a highly homogeneous signal for the 4h to a highly different pattern for the 16h. To bridge the gap between the spectrally and temporally resolved maps, we measured the two peaks and their time dependence simultaneously. To do so, we performed TR-PL Spectroscopy using a streak camera on the 16h spot, and obtained **Figure 4(e).** We see that at short time, emission comes from the range [650-800] nm but a few nanoseconds after the laser pulse, only the main perovskite peak remains (centered at 760nm). More details and cross sections are shown in **Figure S6**.

We attribute this new emission to the formation of a I-poor perovskite, confirmed by quantitative surface chemistry analysis. However, the A-site cation modification could also lead to a change of emission bandgap as recently obtained in perovskite nanocrystals[45]. In **Figure 4(f),** we plot the I : Br, I : (I+Br) and I : Pb ratios as a function of the X-ray exposure time, in comparison with the theoretical stoichiometry (dashed lines). **Figure 4(g)** shows the same ratios but normalised. For the first 1h, the surface seems to be richer in Iodine, compared to the expected theoretical values (I : Br is 7 instead of 5.2 expected). This finding was highlighted in our previous work showing that the Bromine tends to be accumulated at the rear interface with TiO_2[24]. We observe a non-identical reduction of the three ratios with the exposure time: The I : (I + Br) decreases progressively by 10% in 16h of X-ray exposure while the I : Br shows a

drastic decrease up to 50% for the same duration, in agreement with the formation of the I-poor region. This observation correlates with a higher bandgap of emission as evidenced with the PL characterization. As the irradiation time increases, we observed a difference of evolution between the I and Br signals. The photoelectric effect on each atomic level has a level-dependent probability that is governed by the value of the level-specific cross section. In the supplementary **Table S1** we give the values of the sensitivity factors (SF) for all the atomic levels accessible to $Al_{K-\alpha}$ radiation. We notice a very substantial difference between the SF_I and SF_{Br} which indicates that the atoms of I will be subject to a much stronger photo-excitation than that of Br. If we consider also the high sensitivity factor of Pb, we see the bonds Pb-I will be more strongly stressed than the Pb-Br bonds. This can partially explain the initiation of imbalances between the disturbances of the different sub-networks over time.

We observed the same trend with the spatially resolved XPS profiles shown in **Figure 3(c)**. These results show a drastic reduction of the I/Br ratio in the centre of the spot area. Moreover, the new PL emission peak seems to correspond to a continuous range of peak emission wavelengths (see the evolution of the maximum of the second peak in **Figure 4(a)**), i.e. it is compatible with a change of I/Br ratios that could be continuously changing. To confirm, we also investigate the local chemical composition of the spots by SEM-EDX analysis. The maps are shown in **Figure S9 and S10** and indicate that while the Bromine signal does not seem to vary inside and outside the spot, the Iodine ones is greatly reduced inside the spot. As EDX is a bulk technique and XPS a surface technique, we can conclude that surface and bulk show a reduction of the I/Br ratio inside the spot after 16h of exposure.

Therefore, the new emission peak observed in PL analysis should be attributed to a region where Iodine was depopulated following X-ray exposure. This I-poor perovskite region shows fast decays, possibly due to charge transfer to the lower pristine perovskite phase and/or recombination processes.

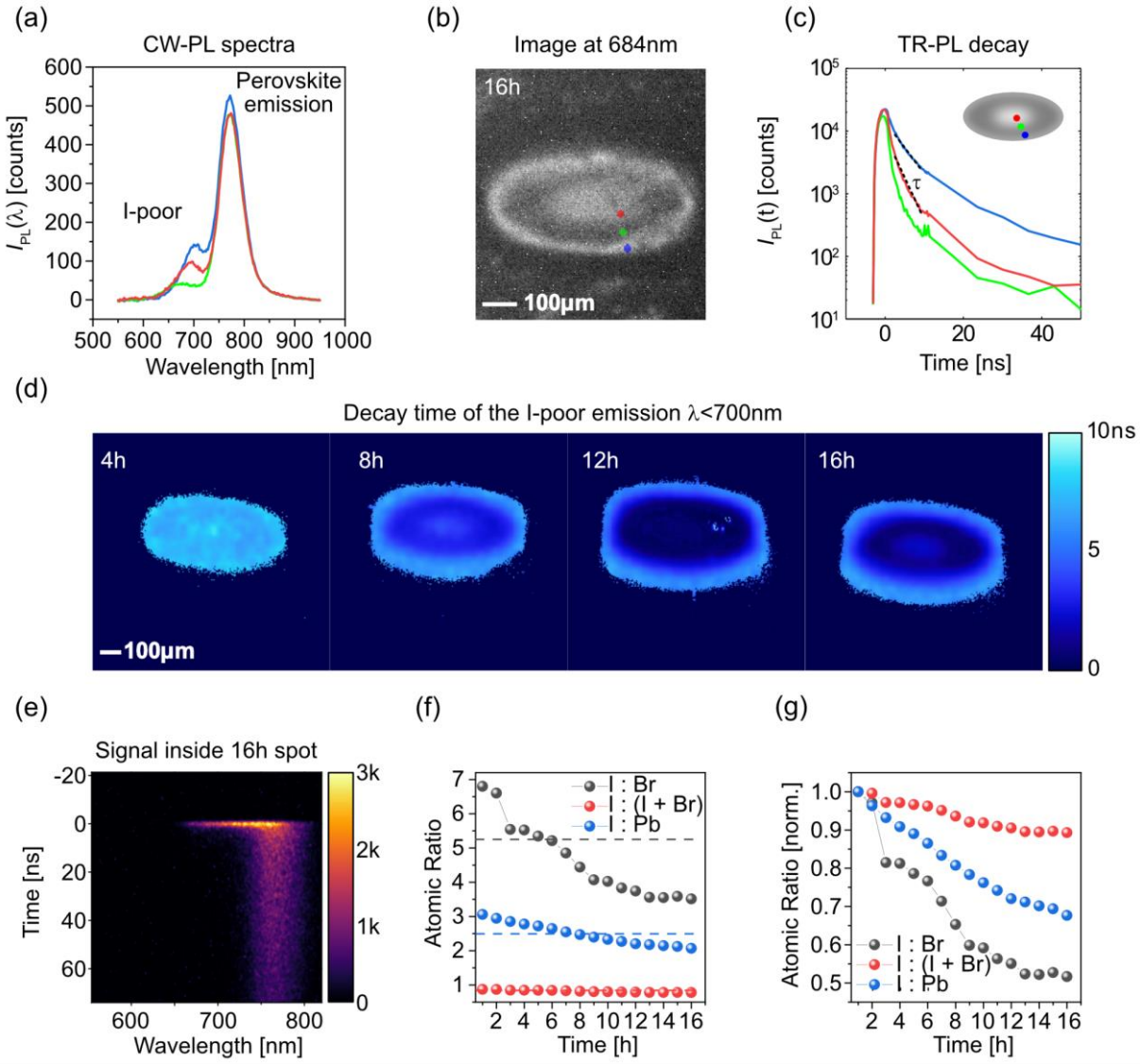

Figure 4: (a) Spectra obtained inside the 16h hour spot in the region shown in (b). (b) cw-PL image at the emission wavelength λ=684nm. (c) TR-PL decays obtained on similar representative regions of interest. (d) Maps of decay time of the 16h spot, computed in the [3,6] ns interval, obtained in the TR-FLIM experiment in the measurement configuration for the emission below 700 nm. (e) TRPL-Spectroscopy acquisition inside the 16h spot (f) Atomic ratios from XPS as a function of exposure time. The dotted lines represent the theoretical stoichiometry. (g) Similar curves, normalised.

Finally, we obtained an estimated formation diagram of the I-poor phase as a function of the X-ray fluence received. To do so, we used the pulsed experiment results, namely the maps of intensity of TR-PL at time t=0ns, $I_{PL}(t=0ns)$ shown in **Figure 5(a)** for the I-poor emission ($\lambda<700nm$) and in **Figure 5(b)** for the perovskite phase ($\lambda>700nm$). We insist that those maps are taken at the exact same positions. We observe that the shape of the $I_{PL}(t=0ns)$ maps evolves greatly with the X-ray exposure time: looking at the 4h and the 16h, we see almost perfectly inverse shapes. This was confirmed over the 4 repetitions of the experiments. As evidenced above, the X-ray spot is not homogeneous meaning that each pixel on a given map corresponds actually to a precise number of X-ray photons received and that each map therefore shows the effects of a distribution of X-ray fluences rather than a unique value. Thus, we can use the space-fluence correspondence (i.e. an image of the X-ray spot intensity) to determine the relative fluence of each pixel of the images. This procedure is described in the SI, in **Figure S7**, we plot the translation and rotation steps, and the iso-line representation. Then, our main hypotheses are the following: one, we assume that the intensity of PL at $t=0ns$ ns $I_{PL}(t=0ns)$ (maps of **Figure 5(a)**) correspond to maps of the local fraction of the I-poor phase; two, we assume that for exposure times below 4h, the local fraction is linearly increasing with the X-ray fluence. Given these two hypotheses, mentioned on **Figure 5(d)**, we plotted the reaction diagram of the I-poor region to the X-ray fluence. We plot it by attributing each pixel of the maps to a local fluence and by using the value of $I_{PL}(t=0ns)$ as a proxy of the local fraction density of the species. Then, we plot the bi-variate histograms with a color scale where a bright color means a higher number of pixels corresponding to both the X-ray fluence (x-position) and I-poor region density or Pristine perovskite density (y-position). We observe in **Figure 5 (d)** an increasing and then a decreasing behaviour for the I-poor fraction after a certain X-ray fluence is reached. On the contrary, the pristine perovskite shows a decreasing only behaviour. This could indicate that the I-poor phase also reacts with X-ray - or is degraded after a too high fluence of X-rays is reached. To check the compatibility of these measurements, we used a toy model in the SI that is able to reproduce qualitatively the observed behaviour and that is shown in dashed red in **Figure 5(d)**. We tested variations of the rotation and translation steps in **Figure S7** and found qualitatively similar curves. The precise chemical reactions cannot be determined by our imaging technique. However, we conclude from this simplified model that our results are compatible with degradation patterns where the I-poor phase seems to also react with X-ray.

To correlate with the degradation of the organic compounds occurring on the extreme surface, we plot in **Figure 5(e)** the normalised N : (I+Br), N : Pb and N : I ratios calculated from the XPS surface composition as a function of the exposure time. We clearly observe the severe decrease of these 3 ratios, similarly, up to 70% in 16h, meaning that the organic species does follow a similar trend as the one obtained with the PL technique. Namely, this validates our interpretation of $I_{PL}(t=0ns)$ as a proxy of the local fraction of the species. Therefore, our PL and XPS analysis suggests that the I-poor perovskite phase that is formed also reacts and or is degraded via X-ray exposure.

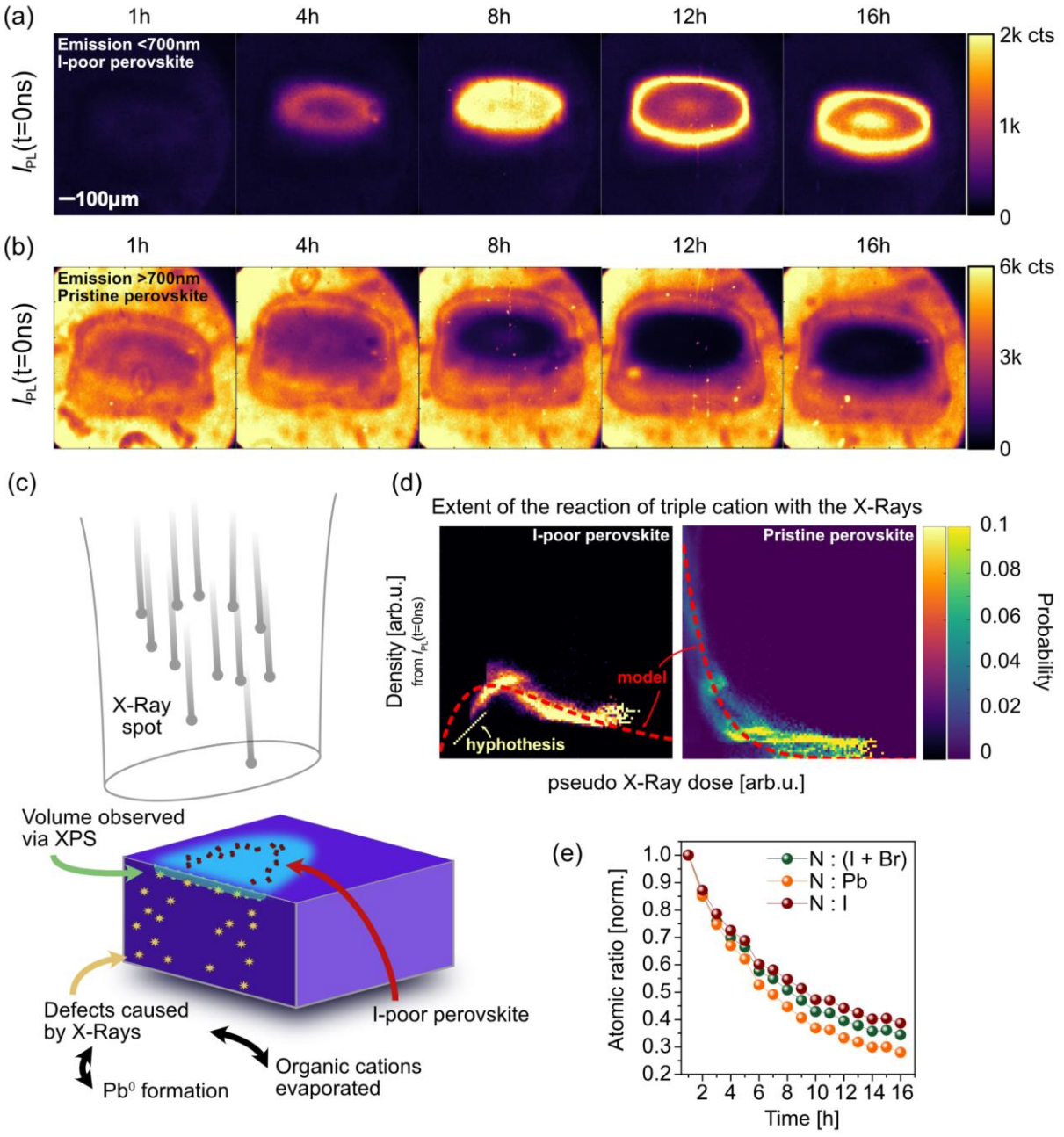

Figure 5: (a) Maps of intensity of I_{PL}(t=0ns) from the TR-FLIM experiment for λ<700nm (b) Similar but for the emission λ>700nm. (c) Scheme of the degradation processes. (d) Plot of the extent of the reaction between X-ray and the formation of the I-poor perovskite as obtained via analysis of the spatial information contained in the I_{PL}(t=0ns) photoluminescence images. Red dotted lines are the model given in SI for the parameters $f_{1/2} = 0.5$; $\sigma_1 = 1/12$; $\sigma_2 = 1/50$. (e) Atomic ratios obtained from XPS surface composition, normalised.

3. Discussion

We analysed the degradation caused by X-ray exposure on triple cation lead halide perovskite for irradiation duration from few minutes to 16h, by coupling surface chemical and optical analysis performed by top-notch photoluminescence imaging of the exposed layers at the ~100 µm scale. We identified two key processes as a results of the extensive use of PL imaging and its correlation with XPS. One, at low X-ray fluence (1h of exposure ~10^{13} ph/cm²), the bulk of the perovskite layers is modified with the formation of bulk defects and no notable chemical change of the surface. Two, at higher fluences (>8h of exposure ~10^{14} ph/cm²), chemical changes are observed at the surface of the layer including organic evaporation, Pb^0 formation and increase of the I/Br ratio yielding to an increase of both bulk and surface defects. We evidenced a new PL emission peak that we attribute to I-poor perovskite. Finally, thanks to advanced image treatment, we were able to estimate an extent-of-reaction plot for this new phase and conclude that it is itself reacting with the X-rays and consumed at high fluence.

From a broader perspective, other stressors were reported in the literature as a source of degradation of the perovskite layers: for vacuum based techniques, mainly light, temperature, polarization[38,39], ion sputtering [24,40] and electron beams[41,42]. In particular, there are some similarities between X-ray photo-excitation and electron excitation. Indeed, during exposure to X-rays, the photoelectric effect generates a stationary flow of photoelectrons with initial kinetic energies between 0eV and 1486.6 eV (with present X-ray source), depending on the core level from which the photoelectron is emitted and related to the nature and structure of the irradiated sample. These flows of photoelectrons are locally emitted throughout space. As the X-ray beam penetrates the entire perovskite layer without noticeable temperature increase[44], core level excitation mechanism is occurring inside the whole layer and is the origin of the chemical and electronic perturbations observed. Large amounts of emitted photoelectrons will multi-interact on their paths through inelastic collision and can lose their initial energy inducing perturbations between the electron-beam and the halide perovskites. We can consider these permanent

currents of free electrons to be similar to an electron beam source. Such processes involve the superposition of recombination by emission of fluorescence or/and of electrons coming from Auger recombination. Orri et al.[23] evidenced Iodine segregation towards the grain boundaries during electron beam irradiation and the formation of both $PbBr_2$ and PbI_2 as degradation products at the grain boundaries. In our case, the negative shifts in the core levels of Pb, I and Br suggest the existence of a new phase that can be compared to what was observed by Orri et al. and that could be interpreted as being then PbI_2 or $PbBr_2$. Second, the X-ray flow might induce local heating of the sample that could also induce degradation. In[43] Divitini et al. show Iodine diffusion as a result of in-situ heating samples in vacuum at temperatures up to 250°C. However, the temperatures reached in our experiment are expected to be much lower and the increase of temperature limited to few degrees.[44] Thus we think that the degradation observed is most probably a result of charge de-excitation and charge currents induced by the X-rays' absorption rather than the local resulting heating.

4. Conclusion

In conclusion, we demonstrated that X-ray-based techniques significantly alter the composition and spatial distribution of perovskite layers as well as their optical properties. Hence, caution should be used when exposing perovskite layers to intense X-ray radiation. Moreover, we have shown that the combination of characterization method used could probe and differentiate surface and bulk damage, with both their chemical origin and impact on electrical properties. The kinetics of the degradation process could also be accessed. The same experimental approach might be applied to compositional studies of other beam-sensitive compounds such as metal-organic frameworks or polymeric materials. Other future work should also include testing the impact of the perovskite alloy composition on its stability, as well as probing precisely the progressive creation of bulk defects in the very low fluence (<1h ~10^{13} ph/cm²) regime.

4. Experimental Section

TR-FLIM imaging

TR-FLIM imaging was performed on a home-made setup consisting of a pulsed 532nm laser (repetition rate of 200kHz) at fluences between 10^{10} and 10^{11} ph/cm²/pulse in homogeneous illumination conditions. A longpass dichroic mirror (Thorlabs DMLP650R) and an objective Olympus x10 plan were used to image the sample with a Princeton PiMAX4 EMICCD camera.

Two collection configurations were used to selectively image two parts of the emission spectrum. In configuration 1, three filters were used (Short pass 800nm, Longpass 665 nm and 750 nm) to image the main perovskite peak. In configuration 2, two filters were used (Short pass 700nm, and a Long pass 610 nm) to image the emission of the I-poor perovskite. The samples were measured in a protective atmosphere under an over-pressure of N_2.

Hyperspectral imaging

Hyperspectral imaging was performed with a home-built microscope. The 2D bandpass filtering system used was from company Photon Etc with 5 nm resolution, and the camera used was a 1Mpix silicon-based CCD camera PCO1300. Illumination was realised with a 405 nm LED in homogeneous configuration. A beam splitter was used to separate illumination and collection (Thorlabs DMLP425) as well as a long pass filter at 450 nm. The LED photon flux was measured at 100mW/cm². The samples were measured in a protective atmosphere under an over-pressure of N_2.

XPS

XPS measurements were carried out under ultra-high vacuum (10^{-9} mbar). The XPS spectrometer is a Thermo Electron K-Alpha+ spectrometer using a monochromatic Al-Kα X-ray source (1486.6 eV) with an X-ray spot size of 400 µm. Calibration of the spectrometer was done using Cu and Au samples following the ASTM-E-902-94 standard procedure. A Constant analyzer energy (CAE) mode was used for the acquisition of High energy resolution spectra with a Pass energy of 20 eV and an energy step size of 0.1 eV, without charge compensation. Thermo Fisher scientific Avantage© data system was used for data treatment and peak fitting. The individual peak envelopes were fitted by a Gaussian –Lorentzian (GL30). The estimated flux of X-ray is ~$5x10^{13}$ ph/cm²/s.

Streak Camera

The time-resolved spectroscopy setup is collecting the light in parallel to the TR-FLIM. (PL is excited in a similar way, and the area of detection is determined from the TR-FLIM). The TRPL spectroscopy detector is composed of a Princeton HRS300 coupled to a Hamamatsu C10910 streak camera with a temporal resolution down to 20ps. The spectra were calibrated with a Bentham lamp as reference.

SEM-EDX

The SEM images were acquired by a MERLIN VP COMPACT from Carl Zeiss, and the EDX measurements by a Xflash 6/30 system from Bruker at an acceleration voltage of 15kV.

Samples Fabrication

$Cs_{0.05}(MA_{0.14}, FA_{0.86})_{0.95}Pb(I_{0.84}, Br_{0.16})_{33}$ perovskite layers were synthetized following the same synthesis protocol described in reference[31]: https://doi.org/10.1021/acsami.0c06844.

Acknowledgements

We thank Marion Provost and Armelle Yaiche for depositing the samples. Guillaume Vidon and Pia Dally contributed equally to this work.

References

[1] J.-P. Correa-Baena, A. Abate, M. Saliba, W. Tress, T. Jesper Jacobsson, M. Grätzel, A. Hagfeldt, *Energy & Environmental Science* **2017**, *10*, 710.
[2] Y. Tu, J. Wu, G. Xu, X. Yang, R. Cai, Q. Gong, R. Zhu, W. Huang, *Adv. Mater.* **2021**, *33*, e2006545.
[3] V. Romano, A. Agresti, R. Verduci, G. D'Angelo, *ACS Energy Lett* **2022**, *7*, 2490.
[4] Z.-K. Tan, R. S. Moghaddam, M. L. Lai, P. Docampo, R. Higler, F. Deschler, M. Price, A. Sadhanala, L. M. Pazos, D. Credgington, F. Hanusch, T. Bein, H. J. Snaith, R. H. Friend, *Nature Nanotechnology* **2014**, *9*, 687.
[5] F. Deschler, M. Price, S. Pathak, L. E. Klintberg, D.-D. Jarausch, R. Higler, S. Hüttner, T. Leijtens, S. D. Stranks, H. J. Snaith, M. Atatüre, R. T. Phillips, R. H. Friend, *The Journal of Physical Chemistry Letters* **2014**, *5*, 1421.
[6] H. Wei, Y. Fang, P. Mulligan, W. Chuirazzi, H.-H. Fang, C. Wang, B. R. Ecker, Y. Gao, M. A. Loi, L. Cao, J. Huang, *Nature Photonics* **2016**, *10*, 333.
[7] S. Li, X. Xie, J. Xiong, F. Wang, J. Liu, M. Jiang, *Crystals (Basel)* **2022**, *12*, 1563.
[8] H. Wu, Y. Ge, G. Niu, J. Tang, *Matter* **2021**, *4*, 144.
[9] A. Datta, J. Fiala, S. Motakef, *Sci. Rep.* **2021**, *11*, 22897.
[10] B. Shabbir, J. C. Yu, T. Warnakula, R. A. W. Ayyubi, J. A. Pollock, M. M. Hossain, J.-E. Kim, N. Macadam, L. W. T. Ng, T. Hasan, D. Vak, M. J. Kitchen, J. J. Jasieniak, *Adv. Mater.* **2023**, e2210068.
[11] W. L. Tan, C. R. McNeill, *Applied Physics Reviews* **2022**, *9*, 021310.
[12] S. Béchu, M. Ralaiarisoa, A. Etcheberry, P. Schulz, *Advanced Energy Materials* **2020**, *10*, 1904007.
[13] C. Das, M. Wussler, T. Hellmann, T. Mayer, W. Jaegermann, *Physical Chemistry Chemical Physics* **2018**, *20*, 17180.
[14] S. Svanström, A. G. Fernández, T. Sloboda, T. Jesper Jacobsson, H. Rensmo, U. B. Cappel, *Physical Chemistry Chemical Physics* **2021**, *23*, 12479.
[15] K. X. Steirer, K. Xerxes Steirer, P. Schulz, G. Teeter, V. Stevanovic, M. Yang, K. Zhu, J. J. Berry, *ACS Energy Letters* **2016**, *1*, 360.
[16] L. Yang, H. Zhang, M. Zhou, L. Zhao, W. Chen, T. Wang, X. Yu, D. Zhou, J. Qiu, X. Xu, *J. Phys. Chem. Lett.* **2020**, *11*, 9203.
[17] B. Philippe, B.-W. Park, R. Lindblad, J. Oscarsson, S. Ahmadi, E. M. J. Johansson, H. Rensmo, *Chemistry of Materials* **2015**, *27*, 1720.
[18] T. J. Jacobsson, T. Jesper Jacobsson, S. Svanström, V. Andrei, J. P. H. Rivett, N. Kornienko, B. Philippe, U. B. Cappel, H. Rensmo, F. Deschler, G. Boschloo, *The Journal of Physical Chemistry C* **2018**, *122*, 13548.
[19] U. B. Cappel, S. Svanström, V. Lanzilotto, F. O. L. Johansson, K. Aitola, B. Philippe, E. Giangrisostomi, R. Ovsyannikov, T. Leitner, A. Föhlisch, S. Svensson, N. Mårtensson,

G. Boschloo, A. Lindblad, H. Rensmo, *ACS Applied Materials & Interfaces* **2017**, *9*, 34970.
[20] P. Fassl, V. Lami, A. Bausch, Z. Wang, M. T. Klug, H. J. Snaith, Y. Vaynzof, *Energy Environ. Sci.* **2018**, *11*, 3380.
[21] A. K. Opitz, A. Nenning, C. Rameshan, M. Kubicek, T. Götsch, R. Blume, M. Hävecker, A. Knop-Gericke, G. Rupprechter, B. Klötzer, J. Fleig, *ACS Applied Materials & Interfaces* **2017**, *9*, 35847.
[22] G. F. Samu, R. A. Scheidt, G. Zaiats, P. V. Kamat, C. Janáky, *Chemistry of Materials* **2018**, *30*, 4202.
[23] J. F. Orri, T. A. S. Doherty, D. Johnstone, S. M. Collins, H. Simons, P. A. Midgley, C. Ducati, S. D. Stranks, *Advanced Materials* **2022**, *34*, 2200383.
[24] S. Cacovich, P. Dally, G. Vidon, M. Legrand, S. Gbegnon, J. Rousset, J.-B. Puel, J.-F. Guillemoles, P. Schulz, M. Bouttemy, A. Etcheberry, *ACS Applied Materials & Interfaces* **2022**, *14*, 34228.
[25] W.-C. Lin, W.-C. Lo, J.-X. Li, Y.-K. Wang, J.-F. Tang, Z.-Y. Fong, *npj Materials Degradation* **2021**, *5*, 1.
[26] I. S. Zhidkov, D. W. Boukhvalov, A. F. Akbulatov, L. A. Frolova, L. D. Finkelstein, A. I. Kukharenko, S. O. Cholakh, C.-C. Chueh, P. A. Troshin, E. Z. Kurmaev, *Nano Energy* **2021**, *79*, 105421.
[27] T. Gallet, D. Grabowski, T. Kirchartz, A. Redinger, *Nanoscale* **2019**, *11*, 16828.
[28] K. Hong, K. C. Kwon, K. S. Choi, Q. Van Le, S. J. Kim, J. S. Han, J. M. Suh, S. Y. Kim, C. M. Sutter-Fella, H. W. Jang, *Journal of Materials Chemistry C* **2021**, *9*, 15212.
[29] A. Bercegol, G. El-Hajje, D. Ory, L. Lombez, *Journal of Applied Physics* **2017**, *122*, 203102.
[30] A. Delamarre, L. Lombez, J.-F. Guillemoles, *Applied Physics Letters* **2012**, *100*, 131108.
[31] S. Cacovich, D. Messou, A. Bercegol, S. Béchu, A. Yaiche, H. Shafique, J. Rousset, P. Schulz, M. Bouttemy, L. Lombez, *ACS Applied Materials & Interfaces* **2020**, *12*, 34784.
[32] G. Vidon, Why Do Decays Decay? Transport and Recombination Dynamics of Solar Cells Revealed via Time Resolved Photoluminesence Imaging : Application to Hybrid Perovskites, Institut polytechnique de Paris, **2022**.
[33] G. Vidon, S. Cacovich, M. Legrand, D. Ory, D. Suchet, J.-B. Puel, J.-F. Guillemoles, in *Physics, Simulation, and Photonic Engineering of Photovoltaic Devices X* (Eds.: A. Freundlich, K. Hinzer, S. Collin), SPIE, **2021**.
[34] J. Liang, X. Hu, C. Wang, C. Liang, C. Chen, M. Xiao, J. Li, C. Tao, G. Xing, R. Yu, W. Ke, G. Fang, *Joule* **2022**, *6*, 816.
[35] W. Li, M. U. Rothmann, A. Liu, Z. Wang, Y. Zhang, A. R. Pascoe, J. Lu, L. Jiang, Y. Chen, F. Huang, Y. Peng, Q. Bao, J. Etheridge, U. Bach, Y.-B. Cheng, *Adv. Energy Mater.* **2017**, *7*, 1700946.
[36] A. Fakharuddin, M. Franckevičius, A. Devižis, A. Gelžinis, J. Chmeliov, P. Heremans, V. Gulbinas, *Adv. Funct. Mater.* **2021**, *31*, 2010076.
[37] D. H. Cao, P. Guo, A. Mannodi-Kanakkithodi, G. P. Wiederrecht, D. J. Gosztola, N. Jeon, R. D. Schaller, M. K. Y. Chan, A. B. F. Martinson, *ACS Appl. Mater. Interfaces* **2019**, *11*, 9583.
[38] H.-S. Kim, S. K. Kim, B. J. Kim, K.-S. Shin, M. K. Gupta, H. S. Jung, S.-W. Kim, N.-G. Park, *J. Phys. Chem. Lett.* **2015**, *6*, 1729.
[39] P. Zhao, J. Xu, X. Dong, L. Wang, W. Ren, L. Bian, A. Chang, *J. Phys. Chem. Lett.* **2015**, *6*, 2622.
[40] C. Noël, S. Pescetelli, A. Agresti, A. Franquet, V. Spampinato, A. Felten, A. di Carlo, L. Houssiau, Y. Busby, *Materials* **2019**, *12*, DOI 10.3390/ma12050726.
[41] N. Klein-Kedem, D. Cahen, G. Hodes, *Acc. Chem. Res.* **2016**, *49*, 347.

[42] C. Xiao, Z. Li, H. Guthrey, J. Moseley, Y. Yang, S. Wozny, H. Moutinho, B. To, J. J. Berry, B. Gorman, Y. Yan, K. Zhu, M. Al-Jassim, *J. Phys. Chem. C Nanomater. Interfaces* **2015**, *119*, 26904.
[43] G. Divitini, S. Cacovich, F. Matteocci, L. Cinà, A. Di Carlo, C. Ducati, *Nat. Energy* **2016**, *1*, 15012.
[44] M. E. Stuckelberger, T. Nietzold, B. M. West, Y. Luo, X. Li, J. Werner, B. Niesen, C. Ballif, V. Rose, D. P. Fenning, M. I. Bertoni, *J. Phys. Chem. C Nanomater. Interfaces* **2020**, *124*, 17949.
[45] C. Otero-Martínez, M. Imran, N. J. Schrenker, J. Ye, K. Ji, A. Rao, S. D. Stranks, R. L. Z. Hoye, S. Bals, L. Manna, J. Pérez-Juste, L. Polavarapu, *Angew. Chem. Weinheim Bergstr. Ger.* **2022**, *134*, DOI 10.1002/ange.202205617.
[46] A. D. Wright, J. B. Patel, M. B. Johnston, L. M. Herz, *Adv. Mater.* **2023**, e2210834.
[47] G. Vidon, S. Cacovich, M. Legrand, A. Yaiche, D. Ory, D. Suchet, J.-B. Puel, J.-F. Guillemoles, *Physical Review Applied* **2021**, *16*, DOI 10.1103/physrevapplied.16.044058.